Proceedings of the 9th World Congress on Electrical Engineering and Computer Systems and Sciences (EECSS'23)
Brunel University, London, United Kingdom – August 03-05, 2023
Paper No. ICBES 156
DOI: 10.11159/icbes23.156

Computational Fluid Dynamics Analysis of Blood Flow in Cerebral Mycotic Aneurysms

Asif S[1], B. J. Sudhir[2], B. S. V. Patnaik[1], Ram K. Nekkanti[2], Ganesh Divakar[2], Kesavapisharady Krishnakumar[2], Sam Scaria[2]
[1]Department of Applied Mechanics, Indian Institute of Technology Madras,
Chennai – 600036, India.
asifsainu@gmail.com; bjs@sctimst.ac.in
[2]Department of Neurosurgery, Sree Chitra Tirunal Institute for Medical Sciences and Technology,
Trivandrum - 695011, India.
bsvp@iitm.ac.in

Abstract **-** Mycotic aneurysm is a serious medical condition that, if not treated promptly, can lead to life-threatening complications. The geometry of a cerebral mycotic aneurysm (CMA) is extremely intricate, and each anatomy is unique. Clinical imaging depicting the complicated architecture of the CMA include Digital Subtraction Angiography (DSA) and Computed Tomography Angiogram (CTA). Analysing the hemodynamics inside the complex aneurysm is still challenging. Computational fluid dynamics (CFD) simulation of blood flow in mycotic aneurysms has emerged as a promising method for understanding the hemodynamic parameters that contribute to the formation and propagation of these aneurysms. Calculations based on computational fluid dynamics (CFD) are used to explore the hemodynamic influences on flow characteristics, secondary flow patterns, and helicity in complex aneurysms. Aneurysm initiation and growth have been widely connected to hemodynamics-based wall shear stress (WSS). The relationship between the hemodynamics of aneurysm initiation and growth that leads to rupture is not entirely established in the context of patient-specific aneurysms. CFD-based studies in CMA are scarce, and the current work fills the gap by employing a patient-specific model.

Keywords**:** Cerebral mycotic aneurysms, CFD, hemodynamic parameters, aneurysm rupture

1. Introduction

Cerebral mycotic aneurysms (CMAs) are rare and potentially life-threatening vascular lesions that occur as a result of bacterial or fungal infections[1]. Intracranial mycotic aneurysms (MAs) are less common than berry aneurysms and are characterized by a focal dilation of the arterial wall due to inflammation, necrosis, and weakening of the arterial wall caused by a showering of bacterial emboli into the circulation[2]. The diagnosis of an infected aneurysm cannot be made using a diagnostic algorithm or criteria, but rather by combining clinical, laboratory, imaging, and surgical results[3]. Mycotic aneurysms are associated with a high incidence of rupture and mortality, which can lead to hemorrhage, sepsis, and death, making early diagnosis and treatment critical[4-7]. Cerebral mycotic aneurysm cases account less than 10% of the Intracranial aneurysms and remaining 90% cases are in a balloon-like enlargement of the vessel lumen[8]. Mycotic aneurysm treatment is difficult and frequently necessitates surgical intervention[9]. The flow dynamics inside mycotic aneurysms are of significant interest to researchers as they may provide insights into the pathophysiology of these aneurysms and inform treatment strategies[10-12].

Computational fluid dynamics (CFD) has emerged as an invaluable tool in the study of blood flow in cerebral aneurysms in recent years, but few studies have focused on CFD of CMAs. Several studies have used different modelling methodologies and computational methods to examine the CFD analysis of blood flow in mycotic aneurysms. The complicated geometry of mycotic aneurysms, together with the non-Newtonian and pulsatile nature of blood flow, has been shown in these investigations to result in highly non-uniform flow patterns and high wall shear stresses[13-14]. Zhao *et al.* (2019) used patient-specific data from computed tomography (CT) scans to create 3D models of mycotic aneurysms in the aorta, and then used a finite element method to simulate blood flow. The existence of the aneurysm affected the blood flow pattern, resulting in zones of low and high wall shear stress, which could contribute to the aneurysm growth. Yue *et al.* (2022) used a combination of CFD and computational structural mechanics to investigate the effect of thrombus formation on the hemodynamics of

mycotic aneurysms along with other aneurysms in abdominal aortic aneurysms (AAA). They found that the presence of thrombus reduced the velocity of blood flow and altered the flow patterns, which could affect the risk of rupture. Overall, CFD has proven to be an effective method for analysing the hemodynamics of mycotic aneurysms, providing vital insight into the underlying mechanisms that lead to their genesis and evolution. Based on the preceding literature, CFD analysis on CMA has not been reported and the current study investigates the flow inside the cerebral mycotic aneurysm with computational fluid dynamics.

2. Methods

This section explains the solution methodology for patient-specific middle cerebral artery (MCA) and cerebral mycotic aneurysm blood flow simulations. To begin, the necessary scanning data from the recruited patient's radiological scans were gathered. These image slices are registered to generate the patient-specific 3D flow domain of interest. The 3D volume is then imported to create the geometric model, meshing, and numerical simulations.

2.1. Case Presentation

A 66-year-old male with a history of chronic alcohol use and with no other co-morbidities presented with history of acute onset weakness in right upper limb and lower limb with slurring of speech with deviation of angle of mouth to left side. He had no history of headache, vomiting or seizure. With these complaints he was evaluated with imaging which showed infarct in left parietal region and aneurysm in the of left M3 segment of MCA. The patient underwent further imaging studies, which revealed irregularly walled fusi-saccular aneurysm involving proximal M3 branches of left MCA likely infective in etiology. Hypodense plaque with eccentric calcification was present in right carotid bulb causing approximately 60% luminal narrowing. Atherosclerotic plaque seen in left carotid bulb causing <50% narrowing. The patient underwent left pterional craniotomy and excision of aneurysm.

2.2. Image acquisition and modelling

A 3D model of a CMA of the respective patient was constructed based on medical imaging data (Computed Tomography (CT) scan) using the software 3D Slicer. The model included the aneurysm sac, inflow and outflow vessels as shown in Fig. 1(a). The generated model was then exported to ANSYS ICEM CFD to generate mesh. The generated mesh is shown in fig. 1(b).

Fig. 1(a): Geometry and 1(b): Mesh

2.3. Governing equations

The generated mesh then subjected to a transient-state CFD simulation using the finite volume method by the commercial software ANSYS Fluent. The three-dimensional patient-specific aneurysm model takes pulsatile in-flow into account in addition to incompressible, laminar, and non-Newtonian blood flow. It is considered that the aneurysm walls are smooth and rigid. Eqs. (1) and (2) give the continuity and Navier Stokes equations, respectively.

Continuity equation:

$$\nabla \cdot \boldsymbol{u} = \mathbf{0} \tag{1}$$

Navier Stokes equation:

$$\boldsymbol{\rho}\left(\frac{\partial \boldsymbol{u}}{\partial \boldsymbol{t}} + (\boldsymbol{u}\cdot\nabla)\boldsymbol{u}\right) = -\nabla \boldsymbol{P} + \nabla \cdot \boldsymbol{\tau} \tag{2}$$

Where ρ denotes the density of the fluid, u is the fluid velocity vector, P is the pressure, and $\boldsymbol{\tau}$ is the stress tensor.

$$\boldsymbol{\tau} = \boldsymbol{\mu}(\dot{\gamma})\frac{\mathbf{1}}{\mathbf{2}}(\nabla \boldsymbol{u} + \nabla \boldsymbol{u}^{\boldsymbol{T}}) \tag{3}$$

μ is the viscosity or apparent viscosity of the fluid and it is a function of shear rate for non-Newtonian fluid. Blood flow was modelled as a non-Newtonian (Carreau model), Eq. (4) expresses the shear-thinning behaviour of blood, which is represented by the Carreau model.

$$\boldsymbol{\mu} = \boldsymbol{\mu}_{\infty} + (\boldsymbol{\mu}_{\mathbf{0}} - \boldsymbol{\mu}_{\infty})[\mathbf{1} + (\boldsymbol{\lambda}\dot{\boldsymbol{\gamma}})^{\mathbf{2}}]^{\frac{\boldsymbol{n}-\mathbf{1}}{\mathbf{2}}} \tag{4}$$

Where μ_0 represents the viscosity at zero shear rate, μ_∞ represents the viscosity at an infinite shear rate, λ is the relaxation time, $\dot{\gamma}$ is the shear rate, and n is the power-law index. The parameters used in the study were gathered from the literature[15], specified as $\mu_0 = 0.056$ Pa.s, $\mu_\infty = 0.0035$ Pa s, $\lambda = 3.313$ s, and $n = 0.3568$, respectively.

2.4. Boundary conditions

2.4.1. Inlet - Time-varying velocity pulse

In the current study, Transcranial Doppler (TCD) was used to investigate the temporal fluctuation of velocity in the Middle Cerebral Artery (MCA) at the inlet of MCA aneurysm models, as shown in Fig. 2(a). Fourier series were used to simulate the temporal fluctuations of the physiological velocity inlet condition, which were then implemented using a user defined function (UDF) script.

2.4.2. Outlets - Time-varying pressure

The time-varying pressure at outlets must be incorporated to adequately reflect the distal resistance of vessels[16]. In this study, we adopted a pulsatile pressure boundary condition at all aneurysm outputs (Fig. 2(b)). The pulsatile pressure boundary condition was developed from previous research and used to aneurysm outlets[17-19]. Using time-varying pressure profiles at outlets results in a more physiological approximation of boundary conditions and blood flow that is closer to the in vivo nature.

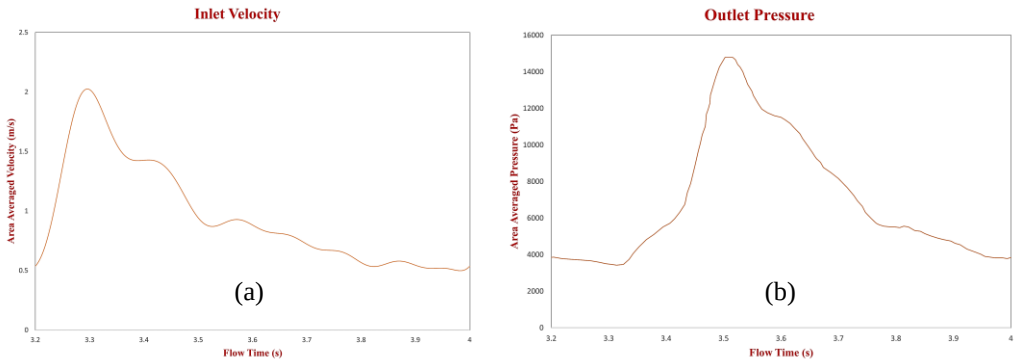

Fig. 2(a): Inlet velocity and 1(b): Outlet pressure

2.5. CFD Analysis

In the CFD analysis, the Navier-Stokes equations were used to describe the motion of a fluid in terms of velocity, pressure, density, and viscosity. Fig. 2(a) shows how the model was set up to simulate blood flow under physiologically relevant settings with a pulsatile velocity. To simulate the resistance of downstream vasculature, the vessel walls were subjected to a no-slip boundary condition, and the outlet boundaries were subjected to a transient pressure boundary condition, as illustrated in fig. 2(b). In this study, the finite volume technique (FVM) was used with ANSYS Fluent and the implicit solver to solve the governing equations and estimate the time-dependent flow through three-dimensional CMA geometry. A second-order implicit scheme is used for transient formulation. For spatial discretization, a second-order upwind approach was used, and the COUPLED scheme was used for pressure-velocity coupling. Each pulse cycle was divided into 800 time steps with a step size of 0.001 s. The convergence criteria for the solutions were considered at a residual value of 10^{-5} for the continuity and the velocity. The simulation has conducted for five cardiac cycles and the presented results were taken from the last cardiac cycle.

An unstructured mesh is used to discretize the flow domain of interest. To capture the complex flow behaviour in these places, the mesh is refined closer to the bifurcation and aneurysm regions. To capture high-velocity gradients, the five inflation layers are used near the wall. The model is subjected to a mesh independence investigation with four different mesh densities[19]. The difference in WSS values between the two meshes was determined to be less than 1%. As a result, the final mesh is used for simulations with 6.94 million elements.

3. Results and Discussions

The CFD simulation gives a detailed information on the flow patterns and hemodynamic characteristics of the CMA. The CFD analysis revealed that the blood flow in the mycotic aneurysm was characterized by complex flow patterns, including recirculation and flow separation. Flow patterns, wall shear stress profiles, and three-dimensional vortices were studied. The peak velocity inside the aneurysm was significantly lower than the peak velocity at the adjacent normal artery. The low velocity in the aneurysm was associated with a higher risk of thrombosis and embolization. The simulation revealed a complex flow pattern with a region of stagnant flow within the aneurysm sac, which has been linked to an increase in thrombosis risk and subsequent rupture.

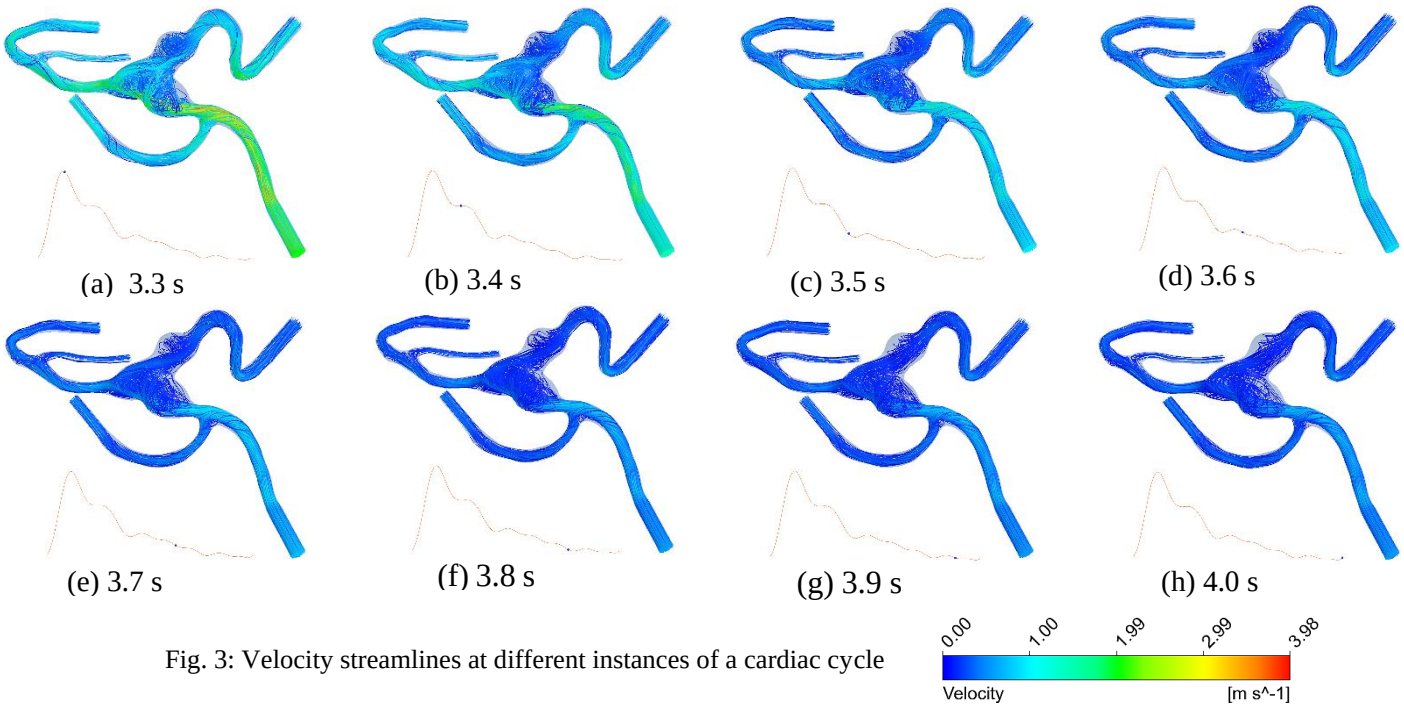

Fig. 3: Velocity streamlines at different instances of a cardiac cycle

In addition, the results showed that the hemodynamic parameters within the aneurysm were dependent on the aneurysm geometry and size. Fig. 3(a-f) shows the velocity streamlines at different instances of a cardiac cycle of the pulsatile flow of blood through mycotic aneurysm and it shows the disturbed flow inside the aneurysm sac. During the systolic phase of the cardiac cycle, maximum velocity can be observed in the curved regions of the inlet vessel and minimum velocity at the aneurysm sac. During the diastolic phase, the velocity is reducing in all regions and nearly a stagnant flow is observed in aneurysm sac. Recirculation strength in the aneurysm is more in the systolic phase than the diastolic phase.

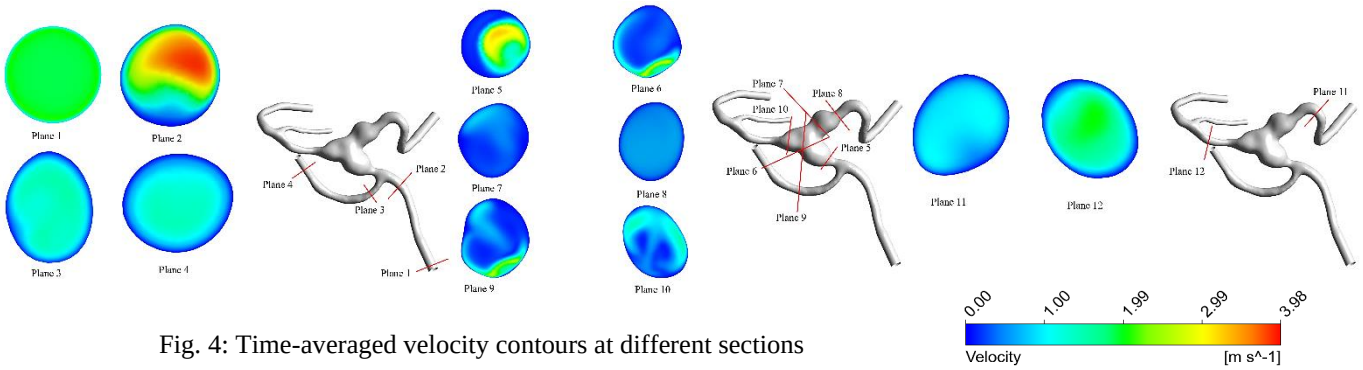

Fig. 4: Time-averaged velocity contours at different sections

Fig. 4 depicts the time-averaged velocity contours at different sections of the geometry. Planes 1-2 are at the inlet vessel and 3-4 are at the outlet vessel before the aneurysm. Planes 5-10 are at the different sections inside the aneurysm. planes 11-12 are the sections at the outlet vessels of aneurysm. It is observed that a higher magnitude of velocity at the inlet section of the aneurysm and a disturbed flow inside the aneurysm. Higher strength of secondary flow is observed at the planes 9 and 10 compared with other planes in the aneurysm. At the outlet side, traces of secondary flows are diminishing.

Table 1: Reynold's number (Re) and Womersley number (α) at different planes

Planes	Area, A (m^2)	Equivalent diameter, D (m)	Velocity, U (m/s) (Time avg. and area avg.)	Area avg. dynamic viscosity, (Pa.s)	Reynold's No., Re	Womersley number, α
1	3.20107×10^{-06}	0.002019355	0.95893	0.00423	485.2920205	1.41654205
2	2.82269×10^{-06}	0.001896255	1.12465	0.003739	604.538411	1.41470734
3	1.60×10^{-06}	0.00142584	0.552183	0.003823	218.2831009	1.0520076
4	1.67×10^{-06}	0.001458526	0.477113	0.003883	189.9779121	1.06785688
5	4.13×10^{-06}	0.002293788	0.624056	0.003934	385.69303	1.6684022
6	1.94×10^{-05}	0.004970255	0.250189	0.004556	289.3035894	3.35928716
7	1.32×10^{-05}	0.004102477	0.149344	0.004789	135.6115838	2.70453469
8	5.46×10^{-06}	0.002636399	0.253524	0.004207	168.4027145	1.85432361
9	1.93×10^{-05}	0.004963626	0.247539	0.004381	297.2865524	3.42121443
10	5.23×10^{-06}	0.002580816	0.304468	0.004016	207.3824194	1.8578414
11	3.53×10^{-06}	0.002119344	0.37684	0.004043	209.4098192	1.5206725
12	1.66×10^{-06}	0.001454302	0.634601	0.003834	255.1559162	1.07150618

Womersley number (α) is expressed as

$$\boldsymbol{\alpha = d\sqrt{\frac{\omega\rho}{\mu}}} \tag{5}$$

Where ω represents the frequency of pulsatile flow, and d represents the characteristics length of the vessel.

The area averaged time – average velocity and area averaged dynamic viscosity at all planes have taken from the simulation results and calculated the Reynold's number and Womersley number at the corresponding planes. The results are shown in table 1.

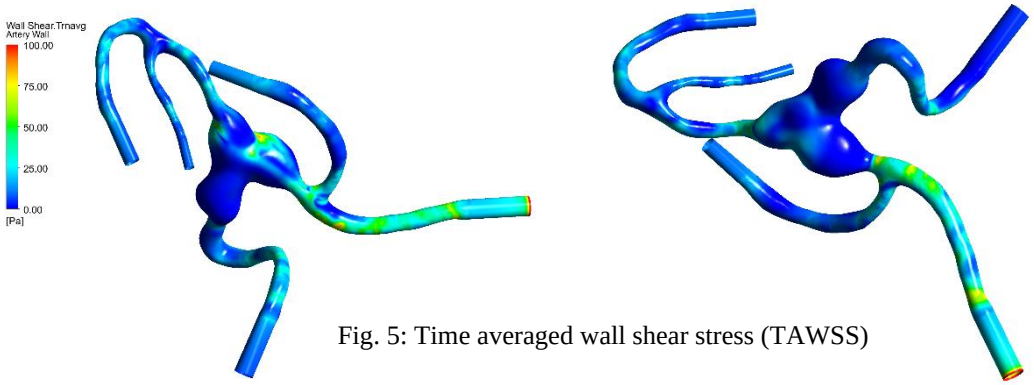

Fig. 5: Time averaged wall shear stress (TAWSS)

The simulation also revealed that the flow was highly disturbed, with areas of low and high wall shear stress. The time averaged wall shear stress (TAWSS) in the vessel wall is shown in fig. 5. Maximum value of TAWSS is occurring at the inlet section of the domain and comparatively very low value of TAWSS can be seen at the aneurysm sac. High value of TAWSS can be seen at some points in the aneurysm. Lower WSS values are connected with aneurysm rupture[20]. High WSS readings, on the other hand, are also linked to aneurysm rupture[21]. Meng *et al.* investigated the aneurysm rupture mechanisms at high and low WSS levels and discovered that aneurysms burst at both high and extremely low WSS levels[22]. Lower TAWSS areas are prone to thrombus formation and aneurysm wall thickening.

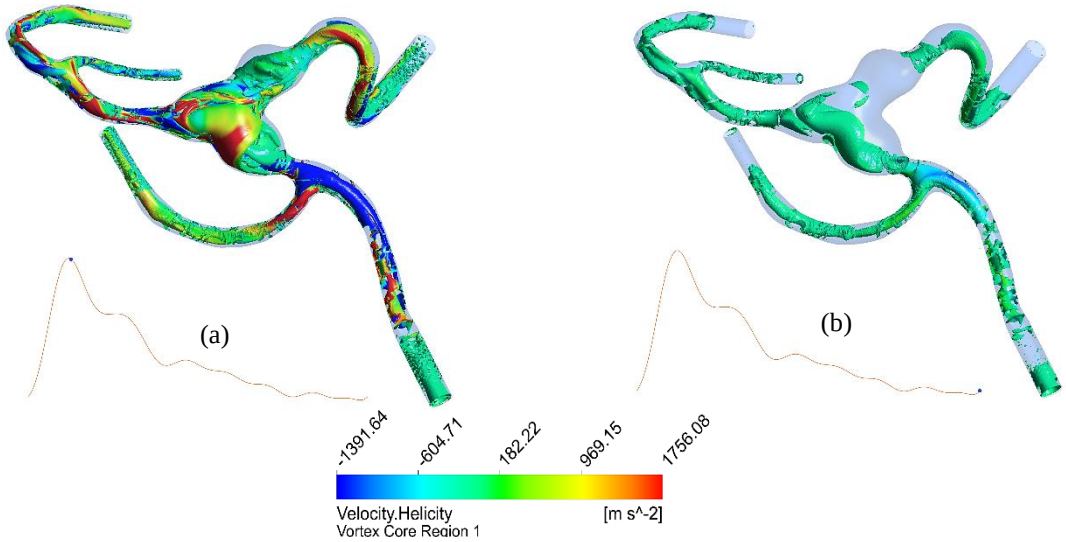

Fig. 6: Three-dimensional structures of helicity (vortex core region with level 0.01) at peak systole and end of diastole

Fig. 6 (a) and (b) shows the helicity plots at the systolic phase and end of diastolic phase respectively. The blue colour represents the anticlockwise rotation of the vortex, whereas the red colour represents the clockwise rotation of the vortex. The strength of helicity is much higher during peak systole than at end diastole. Because of the complicated structure of aneurysm, the vortex size is asymmetric. Near the inlet, the anticlockwise vortex prevails, whereas the clockwise vortex dominates towards the outlet and at one side of the aneurysm. The combination of clockwise and anticlockwise vortices dominates in one outlet where the secondary flow is much higher as shown in fig. 4. At the end of the diastolic phase, the vortex size is much lower compared with peak systole

4. Conclusion

In the present study, patient specific cerebral mycotic aneurysm at the M3 segment of MCA was chosen to study the hemodynamics. It was observed that CFD analysis is a valuable tool for the analysis of the blood flow in mycotic aneurysms. The analysis can provide valuable information about the flow patterns, velocity, wall shear stress distribution and vortex formation in the aneurysm, which can aid in the diagnosis and treatment of the disease. The results of this study shed light on the hemodynamics of CMAs and demonstrate the potential of CFD as a tool for studying this rare and challenging vascular lesion. The results of the current simulation suggest that the formation and progression of mycotic aneurysms are influenced by the non-uniform and complex flow patterns that occur within the aneurysm. The complex flow patterns and disturbed flow in CMAs may contribute to their high risk of rupture and thrombosis. The use of CFD analysis in the management of mycotic aneurysms can help to reduce the risk of complications and improve patient outcomes. These findings may help guide the development of more effective treatment strategies for mycotic aneurysms, as well as improve our knowledge of the underlying mechanisms that contribute to the genesis and progression of these diseases. Further detailed research is needed with more cases to validate these findings and develop strategies to improve the diagnosis and treatment of CMAs.

Acknowledgements

This work was supported by the Science and Engineering Research Board, Government of India, under the Scientific and Useful Profound Research Advancement (SUPRA) scheme (Grant No. SPR/2020/000298).

Conflicts of Interest

There are no conflicts of interest declared by the authors.

References

[1] Sucharita Ray, Neeraj Balaini, Kamalesh Chakravarty, Shivnarayan Pattanayak, Abeer Goel, Aastha Takkar and Vivek Lal, "Special scenarios in the management of central nervous system aspergillosis: a case series and review of literature," *Postgraduate Medical Journal*, vol. 95, pp. 382-389, 2019.

[2] Chapot R, Houdart E, Saint-Maurice JP, Mounayer C, Lot G and Merland JJ., "Endovascular treatment of cerebral mycotic aneurysms," *Radiology*, vol. 222, no. 2, pp. 389- 396, 2002.

[3] Majeed H and Ahmad F. (2023, Feb 12). Mycotic Aneurysm. In: StatPearls [Internet]. Treasure Island (FL):StatPearls Publishing. Available: https://www.ncbi.nlm.nih.gov/books/NBK560736/

[4] Robert G. Hart, Kathleen Kagan-Hallet and Susan E. Joerns, "Mechanisms of Intracranial Hemorrhage inInfective Endocarditis," *Stroke*, vol. 18, no. 6, pp. 1048- 1056, 1987.

[5] Barbara Theresia Müller, Otto Ruano Wegener, Klaus Grabitz, Michael Pillny, Lutz Thomas and Wilhelm Sandmann, "Mycotic aneurysms of the thoracic and abdominal aorta and iliac arteries: Experience with anatomic and extra-anatomic repair in 33 cases," *Journal of Vascular Surgery*, vol. 33, no.1, pp. 106-113, 2001

[6] Florence Y. Chan, E.Stanley Crawford, Joseph S. Coselli, Hazim J. Safi and Temple W. Williams, "In situ prosthetic graft replacement for mycotic aneurysm of the aorta," *The Annals of Thoracic Surgery*, vol. 47, no.2, pp. 193-203, 1989

[7] I-Ming Chen, Hsiao-Huang Chang, Chiao-Po Hsu, Shiau-Ting Lai and Chun-Che Shih, "Ten-Year Experience with Surgical Repair of Mycotic Aortic Aneurysms," *Journal of the Chinese Medical Association,* vol. 68, no. 6, pp. 265-271, 2005
[8] Mannekomba R. Diagbouga, Sandrine Morel, Philippe Bijlenga and Brenda R Kwak, "Role of hemodynamics in initiation / growth of intracranial aneurysms," *European Journal of Clinical Investigation,* vol. 48, no. 9, 2018
[9] Amy R. Deipolyi, Jun Rho, Ali Khademhosseini and Rahmi Oklu, "Diagnosis and management of mycotic aneurysms," *Clinical Imaging,* vol. 40, no. 2, pp. 256-262, 2016
[10] Wai-Kit Lee, Peter J. Mossop, Andrew F Little, Gregory J. Fitt, Jhon I Vrazas, Jenny K. Hoang and Oliver F. Hennessy, "Infected (Mycotic) Aneurysms: Spectrum of Imaging Appearances and Management," *RadioGraphics,* vol. 28, no. 7, pp. 1853-1868, 2008
[11] Andrew Joshua Kobets, Aleka Scoco, Jonathan Nakhla, Allan Leonard Brook, Merritt Drew Kinon, Nrupen Baxi and David Altschul, "Flow-Diverting Stents for the Obliteration of Symptomatic, Infectious Cavernous Carotid Artery Aneurysms," *Operative Neurosurgery,* vol. 14, no. 6, pp. 681-685, 2018
[12] Labib Shahid, James Rice, Haben Berhane, Cynthia Rigsby, Joshua Robinson, Lindsay Griffin, Michael Markl and Alejandro Roldán-Alzate, "Enhanced 4D Flow MRI-Based CFD with Adaptive Mesh Refinement for Flow Dynamics Assessment in Coarctation of the Aorta," *Annals of Biomedical Engineering,* vol. 50, no. 8, pp. 1001-1016, 2022.
[13] Zhao S, Wang Z, Li Y, Wang H and Zhao Y, "Endovascular treatment of multiple tuberculous mycotic aneurysm: A case report," *Medicine (Baltimore),* vol. 98, no. 17, pp. 1-5, 2019
[14] Yue Qiu, Jiarong Wang, Jichun Zhao, Tiehao Wang, Tinghui Zheng, Ding Yuan, "Association Between Blood Flow Pattern and Rupture Risk of Abdominal Aortic Aneurysm Based on Computational Fluid Dynamics," *European Journal of Vascular and Endovascular Surgery,* vol. 64, no. 2-3, pp. 155-164, 2022
[15] K. R. Cho and Y. I. Kensey, "Effects of the non-Newtonian viscosity of blood on flows in a diseased arterial vessel. Part 1: Steady flows," *Biorheology,* vol. 28, no. 3-4, pp. 241-262, 1991.
[16] G. Ogedegbe and T. Pickering, "Principles and Techniques of Blood Pressure Measurement," *Cardiology Clinics,* vol. 28, no. 4, pp. 571-586, 2010
[17] A. Aranda and A. Valencia, "Study on the relationship between wall shear stress and aspect ratio of cerebral aneurysms with different pressure differences using CFD simulations," *Journal of Mechanics in Medicine and Biology,* vol. 18, no. 5, pp. 1850055, 2018
[18] A. Aranda and A. Valencia, "Computational study on the rupture risk in real cerebral aneurysms with geometrical and fluid-mechanical parameters using FSI simulations and machine learning algorithms," *Journal of Mechanics in Medicine and Biology,* vol. 19, no. 3, pp. 1950014, 2019
[19] M.S. Nagargoje, C. Valeti, N. Manjunath, B. Akhade, B.J. Sudhir, B.S.V. Patnaik, and S.K. Kannath, "Influence of morphological parameters on hemodynamics in internal carotid artery bifurcation aneurysms," *Phys. Fluids,* vol. 34, no. 10, pp. 101901, 2022
[20] G. Lu, L. Huang, X. L. Zhang, S. Z. Wang, Y. Hong, Z. Hu, and D. Y. Geng, "Influence of hemodynamic factors on rupture of intracranial aneurysms: Patient-specific 3D mirror aneurysms model computational fluid dynamics simulation," *American Journal of Neuroradioogy,* vol. 32, no. 7, pp. 1255-1261, 2011
[21] J. R. Cebral, F. Mut, J. Weir, and C. Putman, "Quantitative characterization of the hemodynamic environment in ruptured and unruptured brain aneurysms," *American Journal of Neuroradioogy,* vol. 32, no. 1, pp. 145-151, 2011
[22] H. Meng, V. M. Tutino, J. Xiang, and A. Siddiqui, "High WSS or Low WSS? Complex Interactions of Hemodynamics with Intracranial Aneurysm Initiation, Growth, and Rupture: Toward a Unifying Hypothesis," *American Journal of Neuroradioogy,* vol. 35, no. 7, pp. 1254-1262, 2014